Communication

Diamond Photoconductive Antenna for Terahertz Generation Equipped with Buried Graphite Electrodes

Taras Viktorovich Kononenko *, Kuralai Khamitzhanovna Ashikkalieva, Vitali Viktorovich Kononenko [ID], Evgeny Viktorovich Zavedeev, Margarita Alexandrovna Dezhkina, Maxim Sergeevich Komlenok, Evgeny Evseevich Ashkinazi [ID], Vladimir Valentinovich Bukin [ID] and Vitaly Ivanovich Konov

Prokhorov General Physics Institute of the Russian Academy of Sciences, 38 ul. Vavilova, 119991 Moscow, Russia
* Correspondence: taras.kononenko@nsc.gpi.ru

Abstract: It has been shown recently that a photoconductive antenna (PCA) based on a nitrogen-doped diamond can be effectively excited by the second harmonic of a Ti:sapphire laser ($\lambda = 400$ nm). The THz emission performance of the PCA can be significantly increased if a much stronger electric field is created between the close-located electrodes. To produce a homogeneous electric field over the entire excited diamond volume, the laser fabrication of deep-buried graphite electrodes inside the diamond crystal was proposed. Several electrodes consisting of the arrays of buried pillars connected by the surface graphite stripes were produced inside an HPHT diamond crystal using femtosecond and nanosecond laser pulses. Combining different pairs of the electrodes, a series of PCAs with various electrode interspaces was formed. The THz emission of the PCAs equipped with the buried electrodes was measured at different values of excitation fluence and bias voltage (DC and pulsed) and compared with the emission of the same diamond crystal when the bias voltage was applied to the surface electrodes on the opposite faces. All examined PCAs have demonstrated the square-law dependencies of the THz fluence on the field strength, while the saturation fluence fluctuated in the range of 1200–1600 $\mu J/cm^2$. The THz emission performance was found to be approximately the same for the PCAs with the surface electrodes and with the buried electrodes spaced at a distance of 1.4–3.5 mm. However, it noticeably decreased when the distance between the buried electrodes was reduced to 0.5 mm.

Keywords: laser; nitrogen-doped diamond; photoconductive antenna; buried electrodes; graphite

1. Introduction

Electromagnetic pulses in the THz frequency range can interact with solids and molecules, thus resulting in excitations at their resonant frequencies. Hence, intense THz pulses have been found to be a powerful tool for research in the field of condensed matter physics, including studies of the single molecule state, plasmonic, phonon, Rydberg, superconducting states, and other problems [1–5]. Moreover, THz sources have attracted great interest to explore their potential applications in biomedicine [6,7], imaging and security [8–11], and communication [12].

Photoconductive antennas (PCAs) are one of the popular laser-based THz sources [1,13,14]. A typical PCA consists of a DC biased metal dipole antenna patterned on a semiconductor substrate. An ultrashort optical pulse being incident on the antenna gap is absorbed inside the semiconductor and generates photocarriers. The arisen photocarriers are accelerated in the DC bias field, producing a transient photocurrent, which drives the dipole antenna and ultimately re-emits as a THz frequency pulse. PCAs are attractive THz sources because they are very compact, operate at room temperature, display high optical-to-THz conversion efficiency while being pumped with relatively low optical power, and enable the generation of subcycle pulses with relatively high peak powers.

Although the peak electric field of the subcycle THz pulses emitted by large-aperture photoconductive antennas (LAPCAs) can reach up to a few hundred kV/cm [13,15], it is still less than the level provided by the sources based on the laser optical rectification [16] or laser breakdown plasma [17]. The main limiting factors of the PCA technology are the saturation of the emitted THz pulses with high optical pump powers and the electric breakdown occurring when a certain level of the applied bias voltage is exceeded. The last limitation makes the dielectric strength value of the materials used for the fabrication of PCAs important. Diamond seems to be the best choice for generating intense THz radiation [13], as it withstands the record-high electric field of 2000·kV/cm [18]. However, diamond also possesses a much larger bandgap (5.46 eV) than all other semiconductors tested for THz generation with LAPCAs (GaAs, GaN, ZnO, ZnSe, SiC, etc.), so it requires deep ultraviolet radiation for the effective generation of photocarriers. The available fast UV lasers are quite complex setups; therefore, they can hardly be used for table-top THz sources. This explains the low interest in diamond-based PCAs during the last two decades despite the promising results obtained for the LAPCA with interdigitated metal electrodes fabricated on a polycrystalline diamond film, which was excited by an ultrashort-pulsed KrF laser [19].

Recently, it has been shown that substitutional nitrogen in nitrogen-doped diamond is an effective source of photoelectrons excited to the conduction band by the second harmonic of a Ti:sapphire laser (λ = 400 nm) [20,21]. The tested HPHT diamond antenna has demonstrated the maximum THz fluence of 0.007 $\mu J/cm^2$ when the pulsed (10 ns) bias field of 25 kV/cm was applied [20]. A significant rise in the emitted fluence is expected for the higher level of the bias field, which can be obtained for the same bias voltage by applying multiple interdigitated electrodes with a reduced interelectrode distance. This is a standard approach widely used for various materials, including CVD diamond excited by UV pulses [19]; the surface electrodes are usually covered by a dielectric encapsulation layer to increase the breakdown threshold. One should take into account, however, that the absorption depth of the nitrogen-doped diamond at λ = 400 nm typically exceeds 0.25 mm [20,21]; hence, the optical excitation of diamond, as well as the THz generation, take place in a relatively thick layer (>0.5 mm). Evidently, the surface electrodes are not able to create a homogeneous bias field over the entire excited layer if the layer thickness is much larger than the interelectrode distance.

Thus, the fabrication of a high-performance interdigitated LAPCA on the base of the nitrogen-doped diamond, where the interelectrode distance is reduced, at least, down to 0.1 mm, requires the essential modification of the electrode design: the electrodes penetrating deep into the diamond crystal should be produced instead of the standard encapsulated surface electrodes. A promising technique for creating such buried electrodes is the laser microstructuring of diamond bulk based on the local transformation of diamond into graphite [22]. Recently, this technique was applied to fabricate three-dimensional graphite electrodes inside CVD diamond crystals by turning the latter into sensitive and stable detectors of ionizing radiation [23–25].

Here, we report, for the first time, on the fabrication and testing of diamond PCAs with a novel design of electrodes, which potentially allows for the multifold enhancement of the electric field and emission performance for the LAPCA based on nitrogen-doped diamond. The electrodes were formed by the laser microstructuring of diamond bulk and consisted of the regular arrays of buried graphite pillars connected by the surface graphite stripes. Conductive graphite microstructures penetrating deep into the nitrogen-doped diamond crystal are expected to produce a homogeneous bias field over the entire excited diamond volume. Several PCAs with a different interelectrode distance and conductivity of the buried pillars were formed in the same diamond crystal. The energy of the THz pulses generated by each PCA was measured as a function of the laser fluence and bias voltage (pulsed or DC) applied. The dependencies of the THz fluence on the bias field calculated for the PCAs equipped with the buried electrodes were compared with the

reference dependence obtained when the bias voltage was applied directly to the opposite faces of the diamond crystal.

2. Materials and Methods

A high-pressure high-temperature (HPHT) diamond single crystal of Ib type ($3.4 \times 3.5 \times 0.66$ mm^3) was used as a basis for the design of seven PCAs with the buried graphite electrodes. The concentration of substitutional nitrogen in the crystal quantified from a 270 nm absorption band [26] reached ~20 ppm, which was proved earlier [21] to give an intensive THz emission under 400 nm pumping. The absorption depth of the laser radiation in the crystal was estimated at about 0.24 mm at the maximum laser fluence applied.

Each of the seven fabricated electrodes included a surface graphite stripe located on one of the two largest faces of the crystal and an array of 14 buried graphite pillars spaced at a distance of 200 μm from each other. According to Figure 1, the surface parts of the three electrodes *f1–f3* and four electrodes *r1–r4* were situated on opposite faces of the diamond crystal. The surface graphite stripes were formed by multishot irradiation with a KrF excimer laser (λ = 248 nm, τ = 20 ns) at a fluence of 30 J/cm^2 and repetition rate of 50 Hz; a square laser spot of 50×50 μm size moved over the diamond surface at a velocity of 50 μm/s. The typical resistance of the 2.6-mm long and 50-μm wide stripe was about 900 Ohm. An additional pair of ring-shaped surface electrodes was formed on the side faces of the crystal (see Figure 1) by applying similar laser processing.
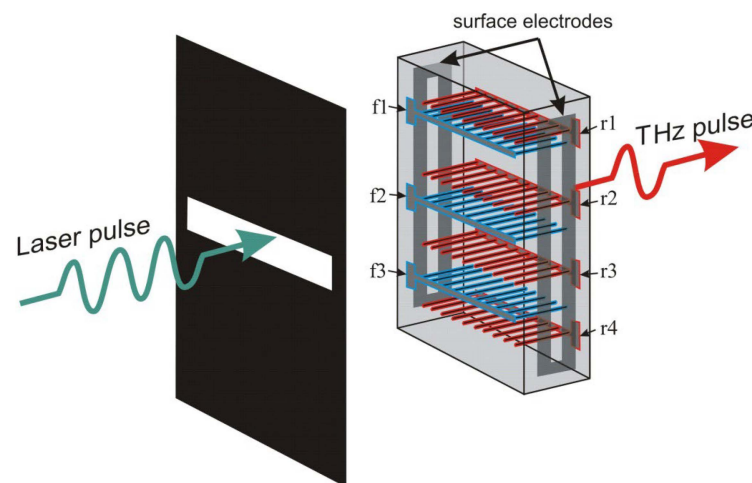

Figure 1. A schematic of graphite buried electrodes formed inside diamond crystal.

Most of the buried pillars were produced with a femtosecond fiber laser HR-Femto (Huaray) emitting 330 fs pulses at a wavelength of 1035 nm and maximum repetition rate of 750 kHz. Before each pillar formation, the crystal was positioned so that the laser beam focused by an aspheric lens with a focal length of 15 mm passed through the crystal and irradiated one of the surface graphite stripes at the rear face. The beam waist was positioned some distance beyond the graphite stripe to initiate the growth of a laser-induced buried pillar on the stripe. The sample was irradiated with a pulse energy of 1.6 μJ and a repetition rate of 3 kHz under the simultaneous movement of the crystal with a constant velocity of 100 μm/s away from the laser. The pillar growth was stopped at a distance of ~ 50 μm before the front crystal face. A typical fs-pulse formed pillar is shown in Figure 2a.

Two of the seven fabricated electrodes (*f3* and *r1* in Figure 1) included the buried pillars produced by a nanosecond laser LS-2132UTF (LOTIS TII) emitting 8 ns pulses at a wavelength of 1064 nm and repetition rate of 15 Hz. The fabrication procedure in this case differed by the pulse energy (10 μJ) and velocity of the crystal movement (0.5 μm/s). The pillars produced by the nanosecond laser caused pronounced damage of the surrounding diamond matrix (see Figure 2b); the occurred microcracks form a specific feather-like structure as all of them were oriented parallel to (111) the diamond planes [27]. However,

the use of nanosecond pulses is known to considerably increase the electrical conductivity of the graphite wires compared with the femtosecond or picosecond pulses [27,28]. A similar trend was observed in the given study: the resistance of 660-µm long pillars formed inside the examined diamond crystal by nanosecond and femtosecond pulses was evaluated as 9 kOhm and 800 kOhm, respectively.
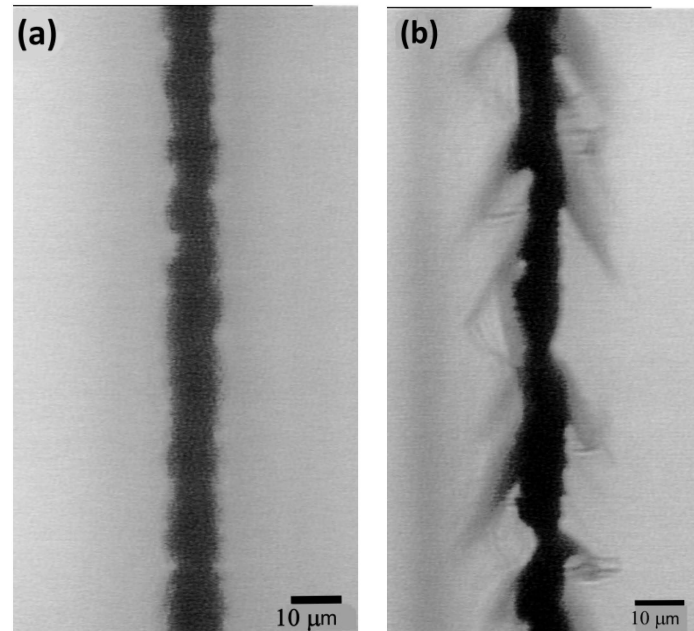

Figure 2. Optical images of buried electrodes formed by laser pulses of different duration: (**a**) 330 fs, (**b**) 8 ns.

Table 1 summarizes the parameters of six PCAs with various electrode interspaces tested in the experiments by applying a bias voltage to particular pairs of the formed electrodes. For the PCAs numbered as #2 and #4–#6, the surface electrodes were situated on different sides of the diamond crystal. This made it possible to apply a higher bias voltage without an electric breakdown, which was crucially important for the PCAs with a small electrode interspace. However, such an electrode configuration complicates the geometry of the electric field inside the crystal near its front and rear faces. To check this effect in terms of THz generation, the PCA #3, with both buried electrodes located at the same crystal face, was examined as well. Thin copper wires were glued to the widened ends of the chosen surface electrodes by a conductive paste. In the case of the PCA #1, the conductive paste covered the whole surface of the side faces.

Table 1. Parameters of the photoconductive antennas.

PCA	Type of Electrodes	Electrode Interspace	Electrode Position
#1	surface	3.5 mm	side faces
#2	buried: f1 + r4 (fs)	2.3 mm	front/rear faces
#3	buried: r2 + r4 (fs)	1.8 mm	rear faces
#4	buried: f1 + r3	1.4 mm	front/rear faces
#5	buried: f1 + r2 (fs)	0.5 mm	front/rear faces
#6	buried: f3 + r1 (ns)	2.15 mm	front/rear faces

The experimental setup for the measurements of the THz emission was reported in detail elsewhere [21]. Optical pumping of the assembled PCAs was performed through the crystal face with three surface electrodes by applying a Ti:sapphire laser system (Spectra Physics) that emitted 0.5 mJ pulses with a ~150 fs pulsewidth at a 800 nm wavelength. Second harmonic radiation (400 nm) was generated with a I-type β-barium borate (BBO)

crystal. The pulse energy was controlled by rotating a half-wave plate combined with a Glan polarizer. Laser radiation passed through a slit in one of the specially prepared opaque screens installed closely in front of the diamond crystal (see Figure 1); the slit width was slightly smaller than the distance between the electrodes used. Two variants of the bias voltage application were tested in the experiments: (1) DC voltage, maximum magnitude of which (up to 2.2 kV) was limited by electric breakdown occurrence and (2) high-voltage pulses (up to 4 kV, ~10 ns full width at half maximum (FWHM)) synchronized with the 1 kHz optical pumping. THz radiation emitted by the PCA was focused by a polytetrafluoroethylene (PTFE) spherical lens (50 mm diameter, f = 60 mm). The collected THz output modulated at 10 Hz was measured by a Golay cell (Tydex GC-1P, aperture of 6 mm, illumination responsivity of $5 \cdot 10^3$ v/w).

3. Results

For all the examined diamond-based PCAs, the experimental dependencies of the THz pulse energy on the pumping optical fluence and bias voltage have been found to be in good agreement with a widely accepted model of THz generation from PCAs [13], which gives the magnitude of terahertz fluence as [29]:

$$F_{THz} = \frac{W_{THz}}{A} = \frac{\tau_{THz} \cdot E_{bias}^2}{2Z_0} \left(\frac{F_{opt}}{F_{opt} + F_{sat}} \right)^2 \tag{1}$$

where W_{THz} is the THz pulse energy, A is the emitting area of the PCA, τ_{THz} is the THz pulse duration, E_{bias} is the applied bias field, $Z_0 \approx 376$ Ohm is the impedance of free space, F_{opt} is the optical fluence, and F_{sat} is the saturation fluence. Figure 3 exemplifies the THz pulse energy as a function of the laser fluence at the fixed bias voltage in the case of the two PCAs with the largest electrode interspaces (d = 3.5 mm and d = 2.3 mm). The results of the experimental data fitting according to Equation (1) (dashed lines) and the evaluated saturation fluence are also shown in Figure 3. The model postulates [13] that the saturation fluence is determined by the pumping optical frequency and parameters of the PCA's material, namely, relative permittivity, reflectivity, and electron mobility. This explains the relatively small stochastic fluctuations of the saturation fluence revealed (Figure 4), as all the examined PCAs formed on the base of the same crystal.
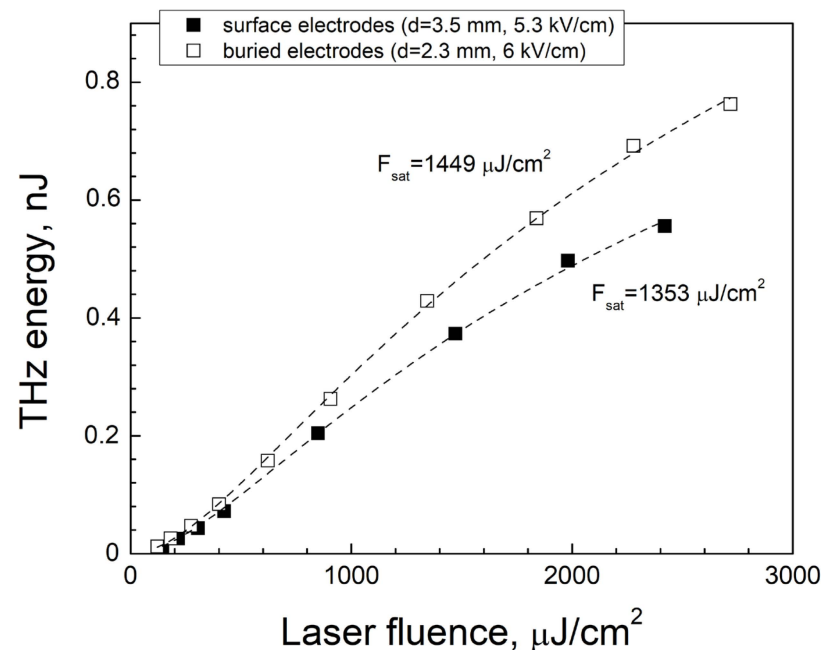

Figure 3. Experimental dependencies of THz pulse energy on laser fluence for PCAs with surface and buried electrodes. Fitting curves according to Equation (1) are shown by dashed lines.
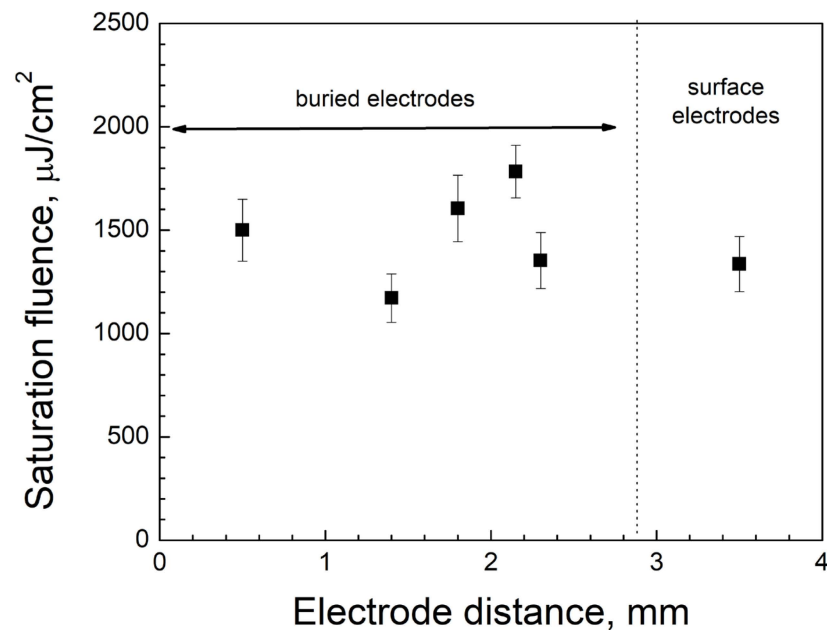
Figure 4. Saturation optical fluence for PCAs with different electrode interspace.

A few examples of the THz pulse energy variation depending on the bias voltage are presented in Figure 5. All datasets were obtained at the fixed optical fluence (F_{opt} = 2500 µJ/cm^2) and can be precisely approximated by parabolic functions (dashed lines) in full accordance with Equation (1). A decrease in the electrode interspace for the PCAs with the buried electrodes (circles and triangles) compared with the surface electrodes on the crystal faces (squares) provides a strengthening of the electric field for the same bias voltage and square-law rise of the THz pulse fluence. Figure 5 also allows for the comparison of the THz emission driven by the DC and pulsed voltage applied for three different PCAs. In the case of the PCA with the surface electrodes (open and closed squares), both variants of biasing give practically the same result (the difference is below 15%). The PCA containing the buried electrodes produced by the femtosecond pulses demonstrates an approximately two-fold increase in the THz signal under the use of the DC voltage (closed circles) instead of the high-voltage pulses (open circles). A similar difference (by a factor of 2–3) was observed for all other examined PCAs equipped with the buried electrodes with the exception of the PCA #6. The electrodes of this PCA were produced by the nanosecond laser pulses and DC bias voltage provided by a relatively small (~25%) excess of the THz emission compared with the high-voltage pulses of the same amplitude. The most probable reason for such a different behavior is the influence of the electrode ohmic resistance on the charging rate of the PCA capacitor. This rate is the lowest for the high-resistance electrodes produced by the fs-pulses, so the oscilloscopic measurements of the HV pulse amplitude performed outside the PCA seem to significantly overestimate the real bias field existing inside the diamond in the moment when the optical pulse arrived.

A well-known advantage of a pulsed bias voltage [30] is the opportunity to reach a larger field strength by avoiding an electric breakdown since the short duration time of the electric field prevents the development of the avalanche ionization. Due to the small size of the diamond crystal and presence of long conductive stripes on its faces, the electric breakdown in air (or over the diamond surface) was observed when the DC bias voltage exceeded the level of 2–2.2 kV. The available HV pulse generator limited the maximum amplitude of the high-voltage pulses by 4 kV. As a result, the HV pulses provided almost a 4-fold gain in the maximum energy of the THz pulses under the use of the ns-pulse formed buried electrodes and only a ~2-fold gain for the fs-pulse formed electrodes (see Figure 5). Let us emphasize that the design of the electrodes was not optimized to apply

the maximum possible bias voltage. The minimum distance over the diamond surface between the employed surface electrodes did not exceed 1.2 mm for all the examined PCAs, also taking into account the ring-shaped graphite electrodes on the side faces (see Figure 1). Burying all the electrode components inside the diamond and removing the graphite stripes from the side faces is expected to increase the DC breakdown voltage by a factor of at least 3.
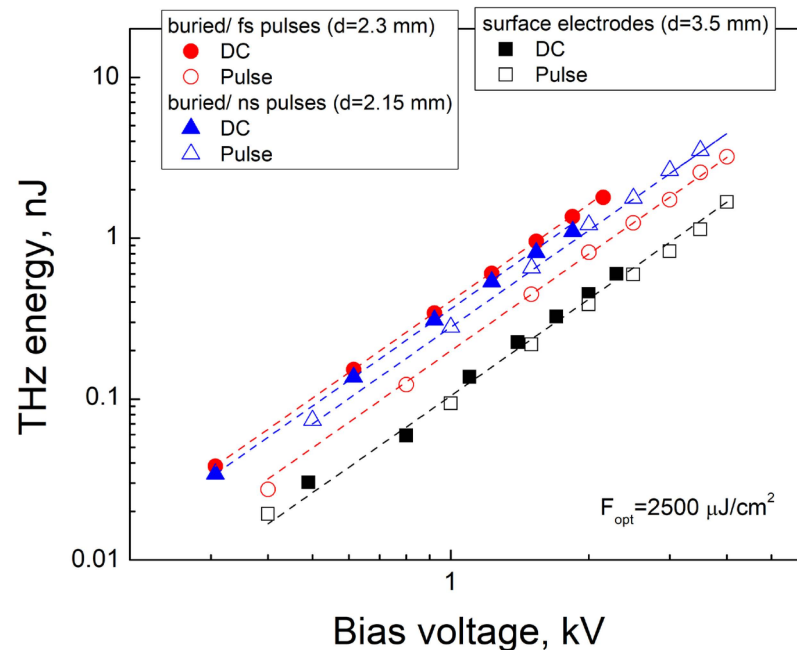

Figure 5. Experimental dependencies of THz pulse energy on bias voltage (DC and pulsed) for PCAs with surface electrodes and buried electrodes formed by fs and ns pulses. Square-law approximations are shown by dash lines.

Taking into account that the variation of the electrode interspace changes the square of the emitting area as well as the electric field strength, it is convenient to compare the emission performance of the different PCAs by analyzing the dependencies of the THz fluence on the electric field strength (Figure 6). As has been expected, all THz fluence dependencies obey the square law and most of them are very close to each other. The only exception is the PCA with the minimum electrode interspace (d = 0.5 mm), which revealed an almost 3-fold decrease in the emitted THz fluence for the same field strength. The reason for such behavior is still not clear. In particular, a similar effect of a decreasing emission performance under the reduction in the submillimeter interelectrode gap in a ZnSe interdigitated LAPCA reported in [31] was explained by the intensification of the space-charge screening effect that caused a significant reduction in the bias field during the THz pulse emission. An important marker of more intensive space-charge screening is the decrease in the saturation fluence that was not observed in our experiments (see Figure 4). Therefore, a few other possible effects are now under investigation. One of those are the spatial inhomogeneities of the bias field in the vicinity of the buried pillars, which have a negative influence on the integral THz signal increases when the electrode interspace decreases. An evident way to diminish this effect is to decrease the period of the pillars' array. Another considered opportunity is the generation of numerous structural defects near the graphite pillars, which trap photocarriers and reduce local THz emission. The latter might become a significant obstacle for designing a diamond-based interdigitated LAPCA with an extra-large field strength and high THz output.
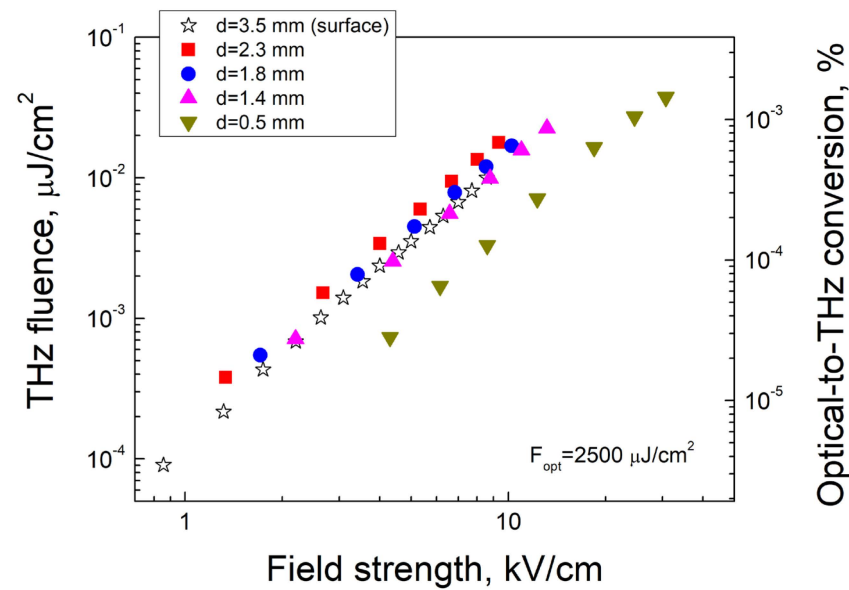
Figure 6. THz fluence as a function of electric field for PCAs with different electrode interspace (DC bias voltage).

4. Conclusions

The arrays of buried conductive pillars formed by the controlled laser-induced graphitization of diamond are shown to be an effective means for the creation of an intense electric field in the entire photo-excited volume of nitrogen-doped diamond crystal. It is proven that the buried graphite electrodes allow for reducing the electrode interspace from 3.5 mm to 1.4 mm without a reduction in the optical-to-THz performance of the diamond PCAs. The revealed decrease in performance for a 0.5-mm gap between the buried electrodes requires further studies. The maximum THz fluence measured for the PCA with the 0.5 mm electrode interspace was 0.04 $\mu J/cm^2$ at a field strength of 30 kV/cm. According to our estimations, burying all the components of the graphite electrodes inside diamond would provide for increasing the DC breakdown voltage for the examined diamond crystal by a factor of 3, which means a rise in the field strength and THz fluence for the above-mentioned PCA up to 90 kV/cm and 0.36 $\mu J/cm^2$, respectively. The last value significantly exceeds the maximum THz fluence reported earlier for the diamond-based PCA pumped by ultrashort UV pulses (0.1 $\mu J/cm^2$) [19] at a close field strength (100 kV/cm).

Institutional Review Board Statement: Not applicable.

Informed Consent Statement: Not applicable.

Data Availability Statement: Not applicable.

Conflicts of Interest: The authors declare no conflict of interest.

References

1. Hafez, H.A.; Chai, X.; Ibrahim, A.; Mondal, S.; Férachou, D.; Ropagnol, S.X.; Ozaki, T. Intense terahertz radiation and their applications. *J. Opt.* **2016**, *18*, 093004. [CrossRef]
2. Chai, X.; Ropagnol, A.; Ovchinnikov, O.; Chefonov, A.; Ushakov, C.; Garcia-Rosas, C.M.; Isgandarov, E.; Agranat, M.; Ozaki, T.; Savel'ev, A. Observation of crossover from intraband to interband nonlinear terahertz optics. *Opt. Lett.* **2018**, *43*, 5463. [CrossRef] [PubMed]
3. Jones, D.Y.; Bucksbaum, P. Ionization of Rydberg atoms by subpicosecond half-cycle electromagnetic pulses. *Phys. Rev. Lett.* **1993**, *70*, 1236. [CrossRef] [PubMed]
4. Nicoletti, D.; Cavalleri, A. Nonlinear light–matter interaction at terahertz frequencies. *Adv. Opt. Photon* **2016**, *8*, 401–464. [CrossRef]
5. Tanaka, K.; Hirori, H.; Nagai, M. THz Nonlinear Spectroscopy of Solids. *IEEE Trans. Terahertz Sci. Technol.* **2011**, *1*, 301–312. [CrossRef]
6. Peng, Y.; Shi, C.; Zhu, Y.; Gu, M.; Zhuang, S. Terahertz spectroscopy in biomedical field: A review on signal-to-noise ratio improvement. *PhotoniX* **2020**, *1*, 12. [CrossRef]
7. Gong, A.; Qiu, Y.; Chen, X.; Zhao, Z.; Xia, L.; Shao, Y. Biomedical applications of terahertz technology. *Appl. Spectrosc. Rev.* **2020**, *55*, 418–438. [CrossRef]
8. Federici, J.; Schulkin, B.; Huang, F.; Gary, D.; Barat, R.; Oliveira, F.; Zimdars, D. THz imaging and sensing for security applications—Explosives, weapons and drugs. *Semicond. Sci. Nd Technol.* **2005**, *20*, S266. [CrossRef]
9. Ren, A.; Zahid, A.; Fan, D.; Yang, X.; Imran, M.A.; Alomainy, A.; Abbasi, Q.H. State-of-the-art in terahertz sensing for food and water security—A comprehensive review. *Trends Food Sci. Technol.* **2019**, *85*, 241–251. [CrossRef]
10. John, T.; Chengjie, X.; Nathan, J.; Kiarash, A.; Navid, A. Review of THz-based semiconductor assurance. *Opt. Eng.* **2021**, *60*, 060901.
11. Castro-Camus, E.; Koch, M.; Mittleman, D.M. Recent advances in terahertz imaging: 1999 to 2021. *Appl. Phys. B* **2022**, *128*, 12. [CrossRef]
12. Koenig, S.; Lopez-Diaz, D.; Antes, J.; Boes, F.; Henneberger, R.; Leuther, A.; Tessmann, A.; Schmogrow, R.; Hillerkuss, D.; Palmer, R.; et al. Wireless sub-THz communication system with high data rate. *Nat. Photonics* **2013**, *7*, 977–981. [CrossRef]
13. Isgandarov, E.; Ropagnol, X.; Singh, M.; Ozaki, T. Intense terahertz generation from photoconductive antennas. *Front. Optoelectron.* **2021**, *14*, 64. [CrossRef]
14. Burford, N.; El-Shenawee, M. Review of terahertz photoconductive antenna technology. *Opt. Eng.* **2017**, *56*, 010901. [CrossRef]
15. Zhang, X.C.; Shkurinov, A.; Zhang, Y. Extreme terahertz science. *Nat. Photonics* **2017**, *11*, 16–18. [CrossRef]
16. Vicario, C.; Jazbinsek, M.; Ovchinnikov, A.V.; Chefonov, O.V.; Ashitkov, S.I.; Agranat, M.B.; Hauri, C.P. High efficiency THz generation in DSTMS, DAST and OH1 pumped by Cr: Forsterite laser. *Opt. Express* **2015**, *23*, 4573–4580. [CrossRef]
17. Oh, T.; Yoo, Y.; You, Y.; Kim, K.-Y. Generation of strong terahertz fields exceeding 8 MV/cm at 1 kHz and real-time beam profiling. *Appl. Phys. Lett.* **2014**, *105*, 041103. [CrossRef]
18. Yoneda, H.; Ueda, K.-i.; Aikawa, Y.; Baba, K.; Shohata, N. Photoconductive properties of chemical vapor deposited diamond switch under high electric field strength. *Appl. Phys. Lett.* **1995**, *66*, 460–462. [CrossRef]
19. Yoneda, H.; Tokuyama, K.; Ueda, K.-I.; Yamamoto, H.; Baba, K. High-power terahertz radiation emitter with a diamond photoconductive switch array. *Appl. Opt.* **2001**, *40*, 6733–6736. [CrossRef]
20. Chizhov, P.A.; Komlenok, M.S.; Kononenko, V.V.; Bukin, V.V.; Ushakov, A.A.; Bulgakova, V.V.; Khomich, A.A.; Bolshakov, A.P.; Konov, V.I.; Garnov, S.V. Photoconductive terahertz generation in nitrogen-doped single-crystal diamond. *Opt. Lett.* **2022**, *47*, 86–89. [CrossRef]
21. Kononenko, V.V.; Komlenok, M.S.; Chizhov, P.A.; Bukin, V.V.; Bulgakova, V.V.; Khomich, A.A.; Bolshakov, A.P.; Konov, V.I.; Garnov, S.V. Efficiency of photoconductive terahertz generation in nitrogen-doped diamonds. *Photonics* **2022**, *9*, 18. [CrossRef]
22. Kononenko, T.V.; Konov, V.I.; Pimenov, S.M.; Rossukanyi, N.M.; Rukovishnikov, A.I.; Romano, V. Three-dimensional laser writing in diamond bulk. *Diam. Relat. Mater.* **2011**, *20*, 264–268. [CrossRef]
23. Oh, A.; Caylar, B.; Pomorski, M.; Wengler, T. A novel detector with graphitic electrodes in CVD diamond. *Diam. Relat. Mater.* **2013**, *38*, 9–13. [CrossRef]
24. Lagomarsino, S.; Bellini, M.; Corsi, C.; Gorelli, F.; Parrini, G.; Santoro, M.; Sciortino, S. Three-dimensional diamond detectors: Charge collection efficiency of graphitic electrodes. *Appl. Phys. Lett.* **2013**, *103*, 233507. [CrossRef]
25. Kononenko, T.; Ralchenko, V.; Bolshakov, A.; Konov, V.; Allegrini, P.; Pacilli, M.; Conte, G.; Spiriti, E. All-carbon detector with buried graphite pillars in CVD diamond. *Applied Physics A* **2014**, *114*, 297–300. [CrossRef]
26. Nistor, V.; Stefan, M.; Ralchenko, V.; Khomich, A.; Schoemaker, D. Nitrogen and hydrogen in thick diamond films grown by microwave plasma enhanced chemical vapor deposition at variable H2 flow rates. *J. Appl. Phys.* **2000**, *87*, 8741–8746. [CrossRef]
27. Ashikkalieva, K.K.; Kononenko, T.V.; Ashkinazi, E.E.; Obraztsova, E.A.; Mikhutkin, A.A.; Timofeev, A.A.; Konov, V.I. Internal structure and conductivity of laser-induced graphitized wires inside diamond. *Diam. Relat. Mater.* **2022**, *128*, 109243. [CrossRef]
28. Lagomarsino, S.; Bellini, M.; Corsi, C.; Fanetti, S.; Gorelli, F.; Liontos, I.; Parrini, G.; Santoro, M.; Sciortino, S. Electrical and Raman-imaging characterization of laser-made electrodes for 3D diamond detectors. *Diam. Relat. Mater.* **2014**, *43*, 23–28. [CrossRef]

29. Reid, M.; Fedosejevs, R. Quantitative comparison of terahertz emission from (100) InAs surfaces and a GaAs large-aperture photoconductive switch at high fluences. *Appl. Opt.* **2005**, *44*, 149–153. [CrossRef]
30. Turton, D.A.; Welsh, G.H.; Carey, J.J.; Reid, G.D.; Beddard, G.S.; Wynne, K. Alternating high-voltage biasing for terahertz large-area photoconductive emitters. *Rev. Sci. Instrum.* **2006**, *77*, 083111. [CrossRef]
31. Ropagnol, X.; Chai, X.; Raeis-Zadeh, S.M.; Safavi-Naeini, S.; Kirouac-Turmel, M.; Bouvier, C.Y.; Côté, M.; Reid, M.; Gauthier, M.A.; Ozaki, T. Influence of Gap Size on Intense THz Generation from ZnSe Interdigitated Large Aperture Photoconductive Antennas. *IEEE J. Sel. Top. Quantum Electron.* **2017**, *23*, 1–8. [CrossRef]